JOURNAL OF GUIDANCE, CONTROL, AND DYNAMICS
Vol. 23, No. 1, January–February 2000

Space-Based Visible Space Object Photometry: Initial Results

R. Lambour,* R. Bergemann,† C. von Braun,‡ and E. M. Gaposchkin§
Lincoln Laboratory, Massachusetts Institute of Technology, Lexington, Massachusetts 02173

One of the objectives of the Midcourse Space Experiment surveillance experiments is to collect photometric and radiometric data on a selected set of resident space objects from the long-wavelength infrared through the short wavelength ultraviolet region of the spectrum. This was done using the Spatial Infrared Imaging Telescope III, Space-Based Visible (SBV), ultraviolet and visible imager, and spectrographic imager instrument packages onboard the spacecraft. Analysis of these data will primarily emphasize 1) construction and validation of phenomenological models for a broad range of resident space object classes, for example, spin- and three-axis stabilized satellites, rocket bodies, and orbital debris, over a wide range of solar phase angles and 2) discrimination between classes of resident space objects and identification of discriminating characteristics within a resident space object class. We concentrate on the initial results from the SBV instrument. We provide an overview of the surveillance data collected to date, discuss its limitations, and present examples of the data collected on two classes of resident space objects.

Nomenclature

A_p = projected area of resident space object, m^2
$B - V$ = stellar color index
M_v = Johnson V-band visual magnitude
M_{SBV} = Space-Based Visual (SBV) magnitude
R = range, m
δ_{sun} = solar declination angle
Ψ = off-specular angle
ψ = Midcourse Space Experiment parallax angle

Introduction

PHOTOMETRY refers to measurement of the light flux from an object, usually in multiple wavelength bands. In the astronomics community, multispectral photometric measurements provide a powerful remote sensing tool to determine the size, shape, rotational period, temperature, and some surface properties of asteroids and comets from reflected sunlight. The same concept can be applied to glean information about Earth-orbiting satellites. The optical signature of a satellite consists primarily of sunlight reflected from various surfaces toward an observer. The reflectivity of the surface depends on wavelength, surface roughness, incident and reflected angles, and temperature. The total signature of the satellite is a function of the satellite configuration, surface material properties, sun–target–observer (phase) angle, and satellite orientation. Satellite photometry has been pursued with varying degrees of enthusiasm since the 1960s, with concentration mainly on the visible wavelengths. These observations have determined quantities of interest such as position, spin period, and variation of brightness with phase angle (phase curve). These quantities can also shed light on the orientation of the satellite, given some a priori knowledge of its configuration.[1–3]

One of the goals of the Midcourse Space Experiment (MSX) surveillance experiments was to collect multispectral photometric data on resident space objects (RSO) for space object identification (SOI) and to investigate its utility for space surveillance. Photometric data from ground-based optical sensors have been a component of the SOI function performed with the space surveillance network for some time. The MSX data are useful for a number of tasks, notably establishment of RSO brightness models to facilitate space surveillance mission planning (scheduling), discrimination, and monitoring. Discrimination refers to the ability to distinguish one RSO from another. Monitoring refers to the task of determining the location and operational status of an RSO. This paper will present additional detail on these concepts and the initial analysis of data from the Space-Based Visible (SBV) sensor.

SBV Overview

The SBV sensor was launched onboard the MSX satellite on 24 April 1996. MSX resides in an 898-km altitude, sun-synchronous orbit. The goal of the SBV was to demonstrate the ability to make observations of RSOs from a space-based platform. The SBV sensor consists of a 15-cm aperture off-axis telescope with a thermoelectrically cooled charge-coupled device (CCD) focal plane (FP). In addition, a signal processor and supporting electronics are also contained onboard the spacecraft. The SBV focal plane consists of four abutted frame transfer CCDs, each with 420 × 420, 27-μm pixels. Additional characteristics of the instrument are presented in Table 1 and in Ref. 4.

The SBV employs two tracking modes to observe RSOs. The primary tracking mode is to track the background stars so that they appear as point sources on the FP. The RSOs will appear as streaks in the FP due to their relative motion with respect to the star field. This mode is known as sidereal tracking. The second mode is to track the RSO so that it appears as a point source while the stars streak on the FP; this is known as ephemeris tracking. Most of the data presented in this paper were obtained in sidereal track mode.

A typical SBV RSO observation consists of 4–16 420 × 420 frames of data. These frames can be stored with the onboard tape recorder and downlinked as raw images, or the images can be processed through the onboard signal processor (SP). The SP extracts relevant information from the raw frames and forms an SP report to be downlinked. The report contains data (position and intensity) on the FP detections that appear as streaks or as point sources. The data presented in this paper were obtained from SP reports rather than reduction of raw images.

The SBV photometric accuracy (Table 1) is characterized in terms of magnitude, where magnitude has the same meaning as it does in the astronomical literature. The magnitude scale is a logarithmic scale that measures relative brightness; for example, a magnitude difference of 5 between two objects corresponds to a factor of 100 difference in brightness. Brighter objects have smaller magnitudes. The photometric accuracy of 0.2–0.3 SBV magnitudes M_{SBV} at $M_{SBV} = 14$ was derived using raw images of Landolt stellar calibration fields.[5] The images were obtained in sidereal track mode, and the point sources were matched with a star catalog to determine

Received 30 November 1998; revision received 14 June 1999; accepted for publication 1 July 1999. This material is declared a work of the U.S. Government and is not subject to copyright protection in the United States.

*Technical Staff Member, Surveillance Techniques Group.
†Consultant, Surveillance Techniques Group.
‡Technical Staff Member and Midcourse Space Experiment Surveillance Principal Investigator; currently Assistant Group Leader and Midcourse Space Experiment Surveillance Principal Investigator.
§Senior Staff Member (retired) and former Midcourse Space Experiment Surveillance Principal Investigator.

Table 1 SBV characteristics

Property	Value
Spectral range	0.3–0.9 μm
Spatial resolution	12.1 arc-s/pixel
Field of view	1.4 × 6.6 deg
Aperture, f-number	15 cm, f/3
Frame integration times	0.4, 0.5, 0.625, 1.0, 1.6, 3.125 s
Frame sizes	420 × 420, 357 × 420, 178 × 420 pixels
Quantum efficiency	28%
Point Source Sensitivity at signal-to-noise ratio = 6.0	15.7 SBV magnitude
Photometric accuracy (point sources)	0.2–0.3 magnitudes at M_{SBV} = 14

Table 2 Principle classes of RSOs observed by SBV

Altitude	Class
Low altitude	Radar calibration spheres
	Stabilized, e.g., DMSP and NOAA[a]
Intermediate altitude	LAGEOS/Etalon spheres
	GPS,[b] GLONASS, Molniya
Deep space	Spin-stabilized cylinders, e.g., HS-376, HS-393, GMS[c]
	Three-Axis stabilized, e.g., HS-601, Gorizont, GE-5000

[a]Defense Meteorological Satellite Program, National Oceanic and Atmospheric Administration.
[b]Global positioning system.
[c]Geostationary Meteorological Satellite.

the identity of each star. Several Landolt fields were imaged, for example SA 106, SA 112, and SA 114. Typically, 12 Landolt stars were used per field for calibration. These stars ranged in magnitude from ~8.5 to 13M_V. Brighter stars were excluded to avoid saturation of the CCD pixels, and dimmer stars were excluded because the signal-to-noise ratio was not adequate for calibration. The color indices of the stars ranged from $0 < B - V < 1.2$ where $B - V$ is simply the difference of the Johnson B-filter and V-filter magnitudes.[6] Smaller $B - V$ values indicate bluer stellar color, and larger numbers indicate redder color (the sun has a $B - V$ value of 0.64). Stars outside this $B - V$ range tend to have little or no flux in the SBV waveband ($B - V < 0$) or have highly uncertain fluxes ($B - V > 1.2$) and were not deemed suitable as calibration objects. An SBV magnitude was determined for each of the calibration stars, and was compared to the published Johnson V-band magnitude M_V for each star to derive the photometric accuracy as a function of M_{SBV}. The photometric accuracy ranges from ~0.05 magnitudes at $M_{SBV} = 9$ to the already stated 0.2–0.3 magnitudes at $M_{SBV} = 14$. The differences between M_{SBV} and M_V will be addressed in a later section.

Note that the photometric accuracy refers strictly to point sources on the FP. When the object of interest appears as a streak on the FP, as is the case with RSO observations in sidereal track mode, the photometric accuracy may degrade. Determination of the photometric accuracy for streaks is in progress. The accuracy stated earlier is useful for preliminary analysis and may be regarded as a best-case accuracy for the sidereal track observations. Consequently, we must be conservative in drawing conclusions from the data.

MSX/SBV Photometric Data Collection Goals and Experiments

The primary goals for SBV photometric data collection were 1) collection of a comprehensive data set for use in definition and validation of phenomenological models of RSOs for space surveillance mission planning and SOI, 2) photometric characterization of a number of different RSO classes and identification of sensor discriminants between and within classes, and 3) collection of data on RSO clusters to investigate the use of photometric data in discrimination and catalog maintenance. Consequently, data are being collected on a number of different RSO classes at a variety of solar phase angles (0–140 deg), including phase angles that cannot be observed from the ground. Table 2 summarizes the principle RSO classes on which data are being collected, and Fig. 1 presents a pictorial comparison of some of these RSO classes. Table 3 presents a summary of the SBV space surveillance experiments; each of these experiments returns some RSO photometric data either through SP reports or raw images. The data discussed in this paper were collected primarily during the SP experiments (SU02, 03, 04, 09, 10, and 15).

As an example of the utility of SBV photometric data, consider the specular search (SU15) experiment. The reflection of sunlight from an RSO consists of two types of reflections characterized as diffuse and specular. The diffuse reflection refers to the omnidirectional reflection of sunlight from the surface and is generally a result of the roughness of the surface. The specular reflection refers to a mirror-like reflection from the surface that tends to be highly directional and significantly brighter. It is the diffuse reflection that permits routine optical detection of RSOs, whereas the specular reflection can be

Table 3 SBV experiment descriptions

Experiment	Description
SU02	RSO detection in high backgrounds
SU03	SBV metric calibration
SU04	Joint SPIRIT III/onboard signal and data processor and SBV metric calibration
SU09	Routine space surveillance tasking
SU10	Geosynchronous belt search
SU11[a]	Unknown object detection and characterization
SU12[a]	Ram/antiram debris observations
SU14[a]	Space object photometry [joint SPIRIT III/SBV or ultraviolet and visible imagers and spectrographic imagers (UVISI)/SBV]
SU15	Search for specular reflections from geosynchronous RSOs
SU17[a]	Space object photometry in stressing backgrounds
SU33[a]	SBV-only or joint SBV/UVISI PI experiment
SU35[a]	Joint SBV/UVISI PI experiment

[a]Raw data collection event.

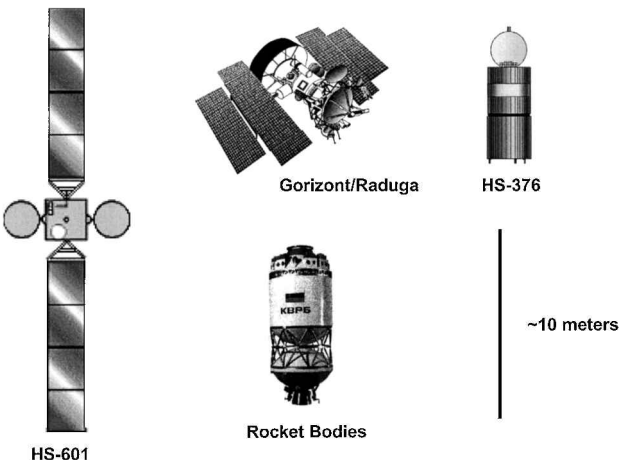

Fig. 1 Representation of RSOs observed by SBV (roughly to scale).

observed at a particular location only when the sun–RSO–observer geometry is appropriate. Specular reflections are observed when the sensor, the normal to the reflecting surface (usually a solar panel), and the sun are in the same plane, and the angle between the sensor and the normal to the reflecting surface is equal to the angle between the sun and the surface normal. The 0.5 deg angular width of the sun is the theoretical width of the reflected ray, but for solar panels, misalignment of the cells broadens this width to a few degrees (Refs. 7 and 8 and R. J. Bergemann, Lincoln Laboratory, Massachusetts Institute of Technology, April 1992, private communication).

For the solar cell covered, spin-stabilized, cylindrical RSOs shown in Fig. 1, the symmetrical distribution of solar cells results in a conical locus of specular reflections about the spin axis, having an angle from the equatorial plane equal and opposite to the sun's declination angle, as shown in Fig. 2. Previous work also indicates that the brightness of the specular reflection varies relatively weakly with phase angle, which means that the specular return can be observed

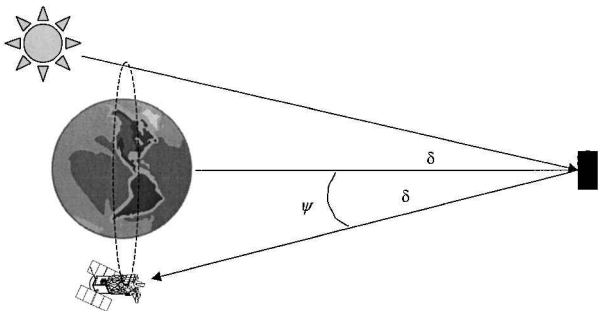

Fig. 2 Specular reflection geometry for spin stabilized RSO (not to scale).

at relatively high phase angles (Bergemann private communication cited earlier).

The SBV can observe the specular return from each of this type of RSO once per orbit when the solar declination is equal or less than the parallax angle ψ, from the geosynchronous belt to the orbit tangent at the MSX polar crossings. The parallax angle ranges between ±10 deg. This geometry permits observation of specular returns for ~50 days, twice per year, centered on the spring and autumnal equinoxes. This is a significant improvement over a stationary, ground-based site, which would be able to observe specular reflections for only a couple of days per year.

The situation is different for the three-axis stabilized payloads. Their solar arrays are essentially flat plates that track the sun; therefore, the phase angles at which the specular reflection from these RSOs can be observed should be extremely limited and dependent on the offset angle between the solar panel normal and the RSO-to-sun vector. Thus, SBV will observe specular returns from these RSOs only at specific phase angles and not necessarily on every orbit.

The utility of the specular data is obvious, for example, 1) spin stabilized and three-axis stabilized payloads can be distinguished from one another based on where and when the specular returns are observed, 2) the misalignment of a spin stabilized RSO spin axis from the equatorial plane can be discerned with multiple observations because the time/location of the peak specular return will be different from the aligned case, 3) solar array offset angles can be determined for three-axis stabilized RSOs allowing determination of available power and age of the spacecraft, and 4) observation of small, otherwise unobservable, RSOs becomes possible.

Initial Data Analysis

The SBV data are presented in units of SBV magnitude M_{SBV}. This is an instrument magnitude and has not been referred to a standardized photometric system. For example, many visible-band astronomical observations are transformed to Johnson V-band magnitude M_V that represents the amount of light flux collected over a wavelength range defined by a Johnson V-band filter, ~505–595 nm (Ref. 6), that allows direct comparison of photometric measurements from different instruments. The SBV is responsive to light over the 300–900 nm region; therefore, magnitudes calculated from SBV measurements are representative of the light flux collected in this waveband and would not necessarily agree exactly with M_V. These magnitude differences may be simply due to the bandwidth difference or perhaps a result of the actual reflected spectrum, that is, color, of the target. SBV is red sensitive when compared to the Johnson V-band and the difference, although not thoroughly investigated, is believed to be less than ~ 0.1–$0.2 M_V$.

The SBV photometric database contained ~28,400 observations of cataloged objects in March 1998. These data represent observations on ~1000 different objects (payloads, debris, and rocket bodies). In our initial survey of the SBV observations we chose to examine the data as functions of phase angle and solar declination angle, that is, season, as was originally done with earlier ground-based observations. Whether or not this is appropriate will become apparent as the data are analyzed. We also chose to consider the data as organized by RSO class. We will present results for two RSO classes, the Hughes HS-376 and the Hughes HS-601.

HS-376 Spin Stabilized

The HS-376 class of satellite is a spin-stabilized cylinder with an Earth-facing antenna mounted on one end (Fig. 1). The cylinder is ~4.7 m in length and ~2.2 m in diameter and is covered primarily with solar cells. The antenna is ~1.8 m in diameter, bringing the total length of the RSO to ~6.6 m. Figure 3 shows the M_{SBV} normalized to a range of 36,000 km vs phase angle for all SBV observations of HS-376 satellites (through March 1998). Active satellites are represented by a black + and inactive satellites by a gray circle. These data represent observations on 42 of the 45 HS-376 spacecraft on orbit in March 1998. The observations range in magnitude from $M_{\mathrm{SBV}} = 8$ to 15, a range of about seven magnitudes. Beavers et al.[3] reported a brightness range of about $6 M_V$, so that it appears that these data are consistent with the previous ground-based measurements. Note the observation of specular reflections ($M_{\mathrm{SBV}} < 10$) at phase angles of ~80 deg. These data suggest that specular data collection on spin stabilized cylinders need not be restricted to low phase angles during the equinoxes. Note that very few of the observations of inactive satellites are brighter than $M_{\mathrm{SBV}} \sim 11$. The inactive spacecraft have orbital inclinations that range from 1 to 9 deg. Additionally, these spacecraft, because their attitude is no longer being actively maintained, may no longer have their spin axes aligned normal to the orbital plane. Both of these effects change the direction of the solar cell surface normal and will move the specular cone to a different location, perhaps ensuring that SBV cannot observe the specular reflection.

There appears to be no well-defined dependence of brightness on phase angle for either the active or inactive cylinders; a wide range of M_{SBV} is observed for any particular phase angle. Several factors may contribute to this. First, we have plotted data from many spacecraft in Fig. 3. However, even if we consider a single spacecraft, a large amount of scatter remains in the data, as shown in Fig. 4. Second, as mentioned earlier, Beavers et al.[3] noted a $6 M_V$ variation in

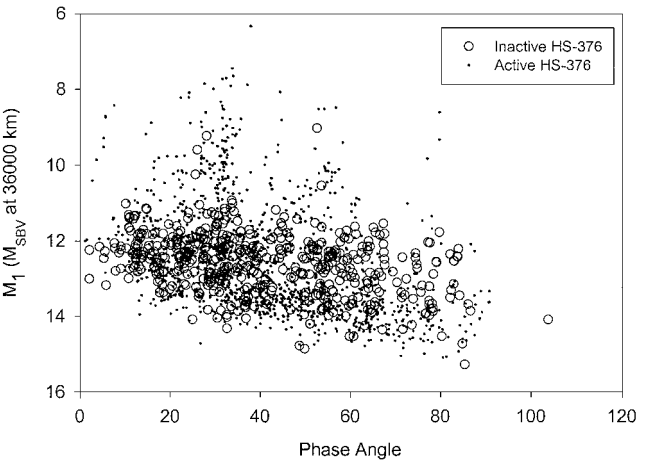

Fig. 3 SBV magnitude as a function of phase angle for HS-376 satellites; total number of observations 1906.

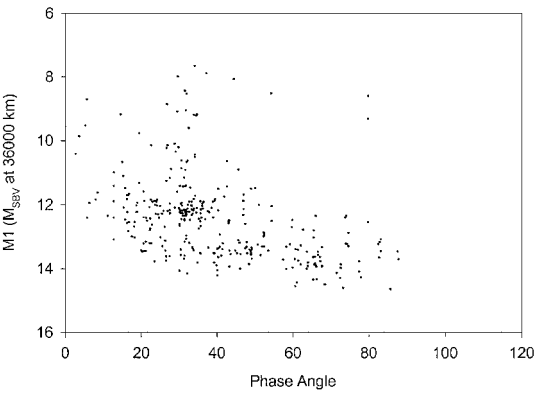

Fig. 4 Phase curve for 20,762 (Thor), an HS-376 spacecraft operated by Norway. Note the bright points at high phase angles.

brightness over the course of a year for some of the HS-376 spacecraft due primarily to the change in solar declination. We plotted the data as a function of solar declination angle δ_{sun} to examine seasonal dependencies in brightness. Figure 5 shows the M_{SBV} as a function of δ_{sun}. For active satellites, which we assume have near-zero orbital inclinations and spin axes parallel to the Earth's spin axis, the sun–target–MSX geometry precludes observation of specular reflections at $|\delta_{sun}| > 10$ deg. Therefore, we expected most of the specular points ($M_{SBV} < 10$) would fall within $\delta_{sun} = \pm 10$ deg. In addition, we expected to observe specular reflections from some of the inactive payloads at $|\delta_{sun}| > 10$ deg due to nonzero inclinations and/or spin axis misalignment. For the same reasons, we expected to observe more scatter in the brightness of the inactive payloads than the active payloads. Figure 5 shows that some of the specular points for the active payloads do fall within $|\delta_{sun}| < 10$ deg, but many do not. In addition, the data on the inactive payloads show much less scatter than the active payloads data and no evidence of specular reflections at $|\delta_{sun}| > 10$ deg. The distribution of data points in Fig. 5 shows that we do not yet have an even distribution of data over season, which may explain why we fail to see the expected pattern.

In Fig. 6, we present the brightness vs δ_{sun} curve for 20762 (Thor spacecraft). It is interesting that we do appear to observe the expected distribution of specular reflections with respect to δ_{sun} for this individual spacecraft. However, there is much more scatter in the data at negative δ_{sun} (fall and winter) than for positive δ_{sun}. If our observing platform were on the ground, we would probably attribute this scatter to glints or reflections off the main antenna that is mounted on the top (north face) of the spacecraft. However, the MSX should be able to observe reflections from the main antenna at any time of the year. Obviously, these trends in the HS-376 data bear further investigation.

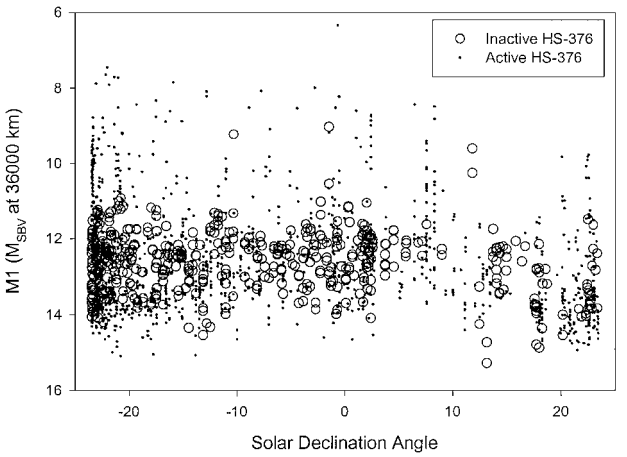

Fig. 5 SBV magnitude as a function of solar declination for HS-376 satellites; total number of observations 1100.

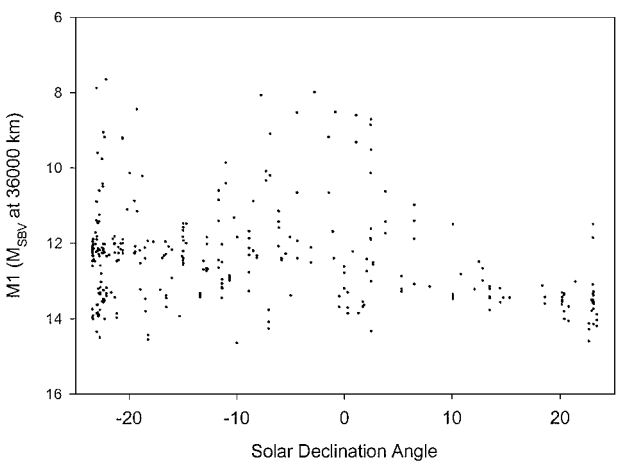

Fig. 6 M_{SBV} vs δ_{sun} for 20,762 (Thor), an HS-376 spacecraft.

The data from the SU15 experiments also prove to be very interesting. In Fig. 7, we present M_{SBV} vs time [universal time (UT)] for a specular search experiment run on 10 April 1997. These data are observations of an RSO cluster consisting of 23877 (Galaxy-9) and 19484 (SBS-5) both of which are HS-376 spacecraft, but of significantly different age (Galaxy-9 was launched in 1996, SBS-5 in 1988). The data show both spacecraft start out fairly bright and then dim by $1–2M_{SBV}$. The spacecraft then brighten again, reaching approximately the same magnitude ($\sim 9.5 M_{SBV}$) at the same time and subsequently dim. The amount of time between the two bright points was ~20 min. Observation of two specular brightenings during a single pass was unexpected; previous models predict a single peak in brightness as the MSX moves through the parallax angle corresponding to δ_{sun} (Bergemann private communication cited earlier).

On 10 April 1997, $\delta_{sun} = 7.96$ deg, which is ~2 deg below the theoretical maximum solar declination at which SBV can observe specular reflections. We believe that MSX passed over the south pole during the time the data were collected and passed through the locus of peak specular brightness (see Fig. 2) twice. Figure 8 facilitates interpretation of the data. Assuming the spin axis of the RSO is aligned with the Earth's spin axis, the MSX will pass through the specular cone, observe a bright reflection, and then the RSO will dim as the MSX moves away from the specular cone. Then, the spacecraft will reenter the specular cone as it moves away from the pole. This model accounts for the two brightenings.

To test this qualitative model, we constructed a semi-empirical brightness model for the HS-376 that explicitly calculates the changing sun–target–MSX geometry. We assume that the target is a geosynchronous spin stabilized cylinder that orbits the Earth in the equatorial plane, with a spin axis parallel to the rotational axis of the Earth. To calculate brightness we begin with an empirical model developed to explain ground-based observations of the older SMS spin-stabilized cylinders (Bergemann private communication cited

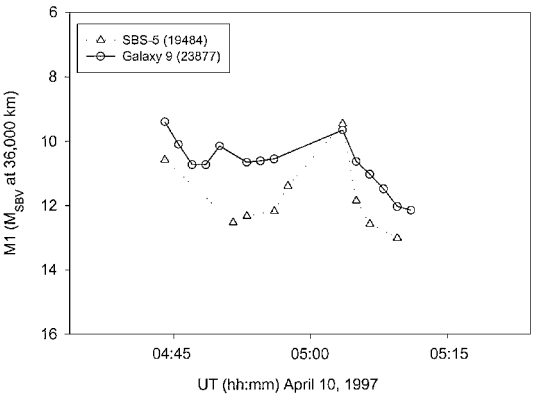

Fig. 7 M_{SBV} vs UT on day 100, 10 April 1997, for 23,877 (Galaxy 9) and 19,484 (SBS-5), two HS-376 spacecraft.

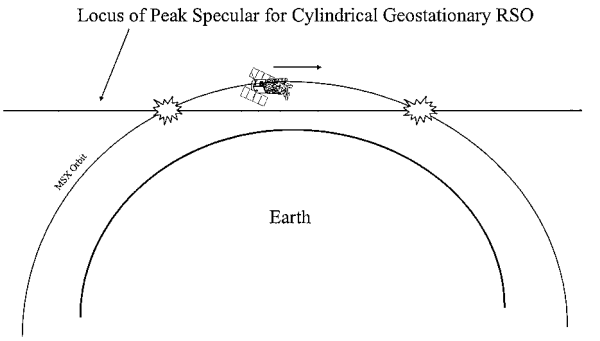

Fig. 8 Geometry that would produce two brightness maxima during the observation of a specular reflection from a cylindrical geostationary RSO; maximum in the RSO light curve occurs at each point where the MSX orbit intersects the locus of peak brightness.

earlier). The visual magnitude of the SMS cylinders is expressed as a function of off-specular angle:

$$M_V = -26.8 - 2.5\log(0.13A_p\Psi^{-1.62}) + 5\log(R) \qquad (1)$$

where Ψ is the difference between the target-to-MSX vector and the angle of peak specular reflection or off-specular angle. This is an angular measure of how far the MSX-to-target geometry is from the peak specular configuration (see Fig. 2). The constant 0.13 primarily represents the reflectivity of the satellite surface. The projected area of the Synchronous Meteorological Satellite (SMS) cylinder is ~ 4 m^2; however, the HS-376 is larger ($A_p = 10.3$ m^2). We have scaled Eq. (1) by the ratio of the HS-376 to SMS areas to derive the following brightness model for the HS-376 class:

$$M_V = -26.8 - 2.5\log(1.093\Psi^{-1.62}) + 5\log(R) \qquad (2)$$

The peak brightness for this model is $M_V = 8.4$, which corresponds well with the peak specular brightness of $M_v = 8.2$ observed from the ground (Ref. 3 and W. Beavers and L. W. Swezey, Lincoln Laboratory, Massachusetts Institute of Technology, October 1995, private communication). We note that this model has no dependence on the right ascension difference between the target and the sun. Essentially, that means that the model brightness is not dependent on how much of the target is illuminated, that is, the phase of the target. For cylindrical targets, this assumption is good for specular reflections out to relatively high phase angles (Bergemann, private communication cited earlier). We also note that neither the SMS or HS-376 cylinder models consider the antenna.

The results from this simple model are presented in Fig. 9. The agreement between the model and the data is quite good for 19484 (SBS-5), and the double peak in the magnitude is reproduced, indicating that our qualitative explanation is correct. In the bottom plot, we see that the model reproduces the phenomenological features of the data, but the agreement between the model and the data for 23877 (Galaxy-9) is not as good; Galaxy-9 appears to be up to two magnitudes brighter than the model predicts. Speculations on the cause for the brightness difference are 1) unknown configurational differences between the two spacecraft and 2) Galaxy-9 spin axis is not perpendicular to the orbit plane as assumed. Galaxy-9 is in a very low inclination orbit; this is not likely to be the cause of the discrepancy. Finally, the difference in brightness could be indicative of an ability to discriminate between RSOs of the same class based on their age, assuming that there are no differences in configuration and that the orientation of both spacecraft are actively maintained as assumed in the model. SBS-5 would presumably be dimmer due to the effects of the space environment on the reflective solar cell surface.

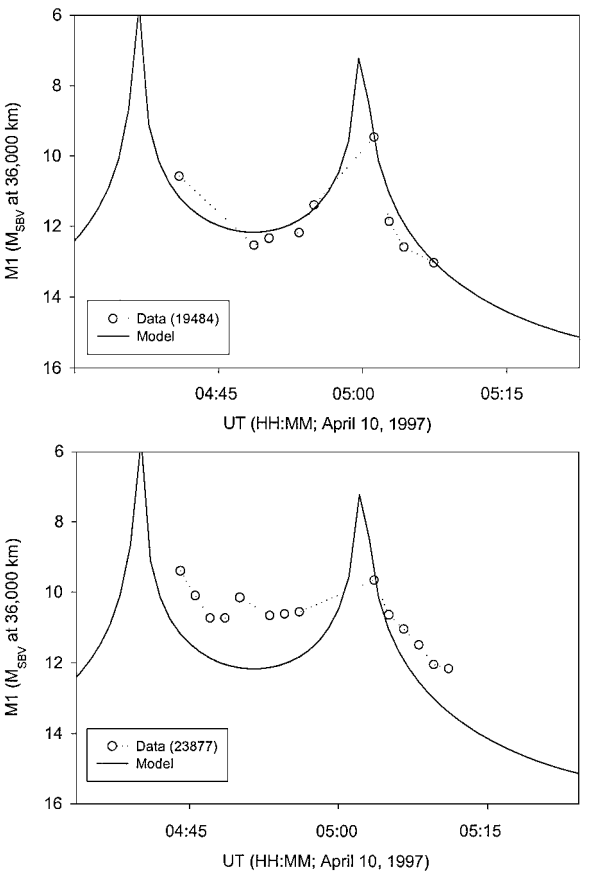

Fig. 9 Comparison of data (black) and model (grey) for SBS-5 (top) and Galaxy-9 (bottom) on 10 April 1997.

HS-601 Three-Axis Stabilized

The HS-601 class is a three-axis stabilized satellite with a central box ($\sim$2.2 m on a side) and two large flat-panel solar arrays on the north and south faces of the box (Fig. 1). The entire spacecraft spans $\sim$21–26 m in length. Figure 10 presents the SBV observations of HS-601 spacecraft in the same format as Fig. 3. Note the dearth of observations on inactive spacecraft; there are 32 HS-601s on orbit and only one of these is inactive. We have three observations on the inactive satellite, making them difficult to distinguish in Fig. 10. Most of the observations (1236 of 1854) in Fig. 10 are of the Direct Broadcast Services (DBS) cluster at 259°E longitude, which contains four HS-601s: 22930 (DBS-1), 23192 (DBS-2), 23553 (Mobil Satellite 2 or MSAT-2), and 23598 (DBS-3). This composite phase curve is well ordered compared to that for the HS-376 class. There is a definite linear trend with respect to phase angle, indicating that it is best to observe these spacecraft at low phase angles. The range of magnitudes observed is $M_{SBV} = 7.5$–15. The specular reflection from the relatively large HS-601 solar arrays is expected to be much brighter than the $M_V \sim 8$ reported by Beavers for the HS-376 class, possibly down to $M_V = 2$–3. The SBV saturates for objects brighter than about $M_{SBV} \sim 8$; therefore, the bright points on the phase curve in Fig. 10 may or may not represent specular reflections. Regardless, there is a general brightening of the class near 30-deg phase angle. This could be indicative of a solar array offset angle of $\sim$15 deg. This brightening implies that data collection for the purposes of determining solar offset angles and, thus, power and age should take place at low (20–30 deg) phase angles for this RSO class.

There appear to be two branches in the phase curve that parallel each other and separate at higher phase angles. Because most of the observations are of the DBS cluster, we examined the data from each of these four spacecraft individually to determine if any of them was responsible for the brighter branch. These data are shown in Fig. 11. The top plot shows the observations of all three DBS satellites and the bottom plot shows the observations for MSAT-2 and MSAT-1 (MSAT-1 is not a member of the DBS cluster but is of the same configuration as MSAT-2 and was included to increase the density of MSAT data points). Obviously, the MSATs are distinguishable from the DBS satellites, having a much flatter phase curve. Why this is so might be due to their radically different configurations; the DBS

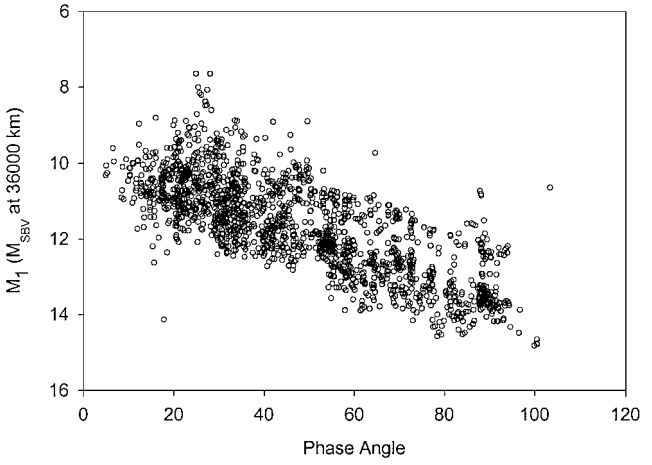

Fig. 10 SBV magnitude as a function of phase angle for HS-601 satellites; total number of observations 1854.

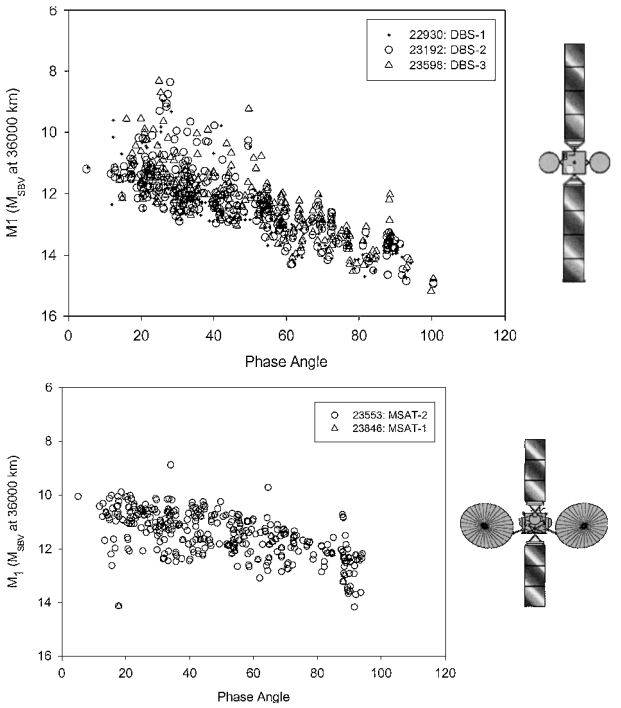

Fig. 11 Comparison of phase curves for satellites in the DBS cluster: observations of the three DBS satellites (top) and MSAT-1 and MSAT-2 (bottom).

satellites consist of a 2.2 m^3 box with two four-panel solar arrays (total area of 43.89 m^2) and two 2.14-m-diam antennas, whereas the MSAT satellites have smaller three-panel solar arrays (total area of 32.92 m^2) and two graphite mesh antennas that measure 4.9 × 6.7 m (Ref. 9). A diagram of each satellite is shown in Fig. 11 (approximately to scale). The MSAT observations are indeed responsible for the brighter branch in the composite phase curve at higher phase angles.

The observations of this spacecraft class may be quite valuable for investigation of sensor discriminants within an RSO class. There are two main configurations for the HS-601, one with three-panel solar arrays and one with four-panel arrays. The difference in area is more than 10 m^2. In addition, the antenna configurations differ significantly for the various satellites.[9] We currently are examining the data for other solar illumination dependencies, differences in brightness based on configuration, and we are constructing a theoretical brightness model for the box and panels satellite configuration to facilitate examination of the data.

Conclusions

We have presented an overview of the SBV sensor, the experiments and methods used to collect visible-band photometric data on various classes of RSOs, for example, payloads, rocket bodies, and orbital debris, and the limitations of these data. Although the photometric error budget remains undetermined for the signal-processed data, we have a best-case estimate for the photometric accuracy and have begun to analyze the data. We have presented examples with preliminary interpretations.

These data are being used to construct and validate resident space object brightness models for use in space surveillance mission planning and for SOI. We touched very briefly on the utility of the data for future surveillance scheduling. Specular reflections from the spin stabilized cylinders can be observed at phase angles of 0–80 deg near the equinoxes that provides a wide window for scheduling observations. Conversely, the three-axis stabilized payloads should be observed at low phase angles to enhance detectability and probability of observing specular reflections from the solar arrays; this provides a narrower window for scheduling observations. Study of the impact of these data on future mission planning is ongoing.

Preliminary comparisons between the HS-376 brightness model developed by Beavers[3] from ground-based data and the SBV data are good, and the SBV data displays similar dependencies with respect to phase angle and season as does the earlier ground-based data. However, it is apparent that the brightness of the HS-376 satellites is not well ordered by phase angle. The SBV data on three-axis stabilized satellites (HS-601) appears well behaved and construction of theoretical brightness models to facilitate examination of the data is underway.

These data will also be used for space object characterization, identification of sensor discriminants, and monitoring tools. The HS-376 specular data and the HS-601 phase curves show some utility for discrimination and monitoring. The HS-376 specular data are particularly interesting in that we apparently observed a significant difference in the magnitude of two cluster members of apparently identical configuration, but differing ages. In addition, we noted a double peak in the light curve for HS-376 specular data taken when the SBV was near the pole when the parallax angle was near the maximum value observable from the MSX orbit. A simple model was developed for the brightness of the HS-376 as a function of off-specular angle, and agreement with the data is good. The ability to obtain two specular returns separated by 0–30 min on every orbit could prove to be a powerful tool for monitoring and maneuver detection. The HS-601 phase curve demonstrated the ability to discriminate between different satellite configurations.

Future work will concentrate on collection of additional photometric data, determination of the photometric accuracy of signal processed data, and continued analysis of the data and application to space surveillance mission planning. In addition to the signal-processed data, the SBV has taken a large amount of raw photometric data on resident space objects that has yet to be analyzed. Addition of these data to the database will also be a priority.

References

[1] Kissell, K. E., "Diagnosis of Spacecraft Surface Properties and Dynamical Motions by Optical Photometry," *Space Research IX*, 1st ed., North Holland, Amsterdam, 1969, pp. 68–70.

[2] McCue, G. A., Williams, J. G., and Morford, J. M., "Optical Characteristics of Artificial Satellites," *Planetary and Space Science*, Vol. 19, No. 8, 1971, pp. 851–868.

[3] Beavers, W., Angione, R., Alten, V., Yanow, K., and Lane, M., "Cylindrical Satellite Specular Season Photometry," *Proceedings of the 1993 Space Surveillance Workshop*, STK-206, MIT Lincoln Lab., Lexington, MA, 1993, pp. 9–18.

[4] Harrison, D. C., and Chow, J. C., "The Space-Based Visible Sensor," *John Hopkins APL Technical Digest*, Vol. 17, No. 2, 1996, pp. 226–235.

[5] Landolt, A. U., "UVBRI Photometric Standard Stars Around the Celestial Equator," *Astronomical Journal*, Vol. 88, No. 3, 1983, pp. 439–460.

[6] Walker, G., *Astronomical Observations: An Optical Perspective*, 1st ed., Cambridge Univ. Press, New York, 1983, pp. 13, 14.

[7] Krag, W. E., "Visible Magnitude of Typical Satellites in Synchronous Orbits," Lincoln Lab., TN 1974-23, Massachusetts Inst. of Technology, Lexington, MA, 1974.

[8] Friedman, A. S., "Determination of Specular Reflection from Cylindrical Satellites for Electro-Optical Surveillance and SOI," Lincoln Lab., Project Rept. ETS-3, Massachusetts Inst. of Technology, Lexington, MA, 1974.

[9] *Jane's Space Directory*, edited by A. Wilson, Jane's Information Group, Alexandria, VA, 1996, pp. 361, 362.